



Functionalization of multi-walled carbon nanotubes and application as supports for electrocatalysts in proton-exchange membrane fuel cell

P. Hernández-Fernández^a, M. Montiel^a, P. Ocón^a, J.L. Gómez de la Fuente^b, S. García-Rodríguez^c, S. Rojas^{c,*}, J.L.G. Fierro^c

^a Dpto. Química-Física Aplicada, Facultad de Ciencias, Universidad Autónoma de Madrid (UAM), C/Co., Tomás y Valiente 7, 28049 Madrid, Spain

^b Department of Materials Science and Engineering, Norges Teknisk-Naturvitenskapelige Universitet (NTNU), C/Sem Sælandsvei 12, NO-7491 Trondheim, Norway

^c Grupo de Energía y Química Sostenibles, Instituto de Catálisis y Petroleoquímica (CSIC), C/Marie Curie 2, 28049 Madrid, Spain

ARTICLE INFO

Article history:

Received 4 May 2010

Received in revised form 30 June 2010

Accepted 6 July 2010

Available online 15 July 2010

Keywords:

Oxygen-containing groups

Multi-wall carbon nanotubes

PEMFC

Oxygen reduction reaction (ORR)

ABSTRACT

The effect of the functionalization degree of multi-walled carbon nanotubes (MWCNTs) on the synthesis and catalytic performance of Pt/MWCNT has been studied. In order to create surface groups of different strengths, MWCNTs have been subjected to either severe or mild oxidation treatment. The experimental data show that increasing metal dispersion is favored on severely treated nanotubes. This is because the treatment provides nucleating sites and enhances the hydrophilicity of the carbon surface. The Pt nanoparticles supported on the MWCNTs subjected to the most severe functionalization treatment gives the best cathode electrode for PEMFC applications, even exceeding the performance of commercial Pt/C. This is due to the higher dispersion of the Pt nanoparticles, as well as a smaller particle size, which is more appropriate for the oxygen reduction reaction.

© 2010 Elsevier B.V. All rights reserved.

1. Introduction

Electrocatalysts for proton-exchange membrane fuel cells (PEMFCs) are based on nanosized Pt particles dispersed onto graphite-type carriers. Reducing the amount of Pt is a key requirement for the implementation of such technology [1], and to this end, several strategies are currently under study. Certain approaches focus on the synthesis of the noble metal phase [2–4], while others deal with the nature of the support [5–8]. Both approaches coincide in the need for increasing metal dispersion, i.e., the amount of Pt (or the adequate noble metal at that) exposed to the reactants [9]. Supporting Pt over an adequate carrier will maximize its surface area while lowering the total amount of material employed [10]. Besides, it is recognized that most reactions of importance for fuel cells are structure sensitive [11]. For instance, it has been established that the catalytic activity of the oxygen reduction reaction (ORR) on Pt-based electrocatalysts depends on the actual size of the Pt particles, finding the maximum activity for particles of around 3.5 nm [12].

In this context, the role of the support becomes very important since it can determine the dispersion and stability of the metallic crystallite, the electronic properties of the electrocatalysts, the mass transfer resistances and the ohmic resistance of the catalyst

layer. When choosing an adequate support for fuel cell applications it should be borne in mind that it should possess high electronic conductivity to support electrochemical reactions, a sufficient specific surface area to accommodate a relatively high metal loading, occasionally exceeding 60 wt%, and a proper pore size distribution. This is without considering stability or degradation issues. Thus far, carbon-based materials, more likely carbon blacks, are the only ones to fulfill such requirements. Several approaches with other materials are being studied, such as conducting polymers [13–15], TiO₂ [4,16], carbon aerogels [17] and carbon nanotubes, to name the most successful ones. Recently, Antolini has published an excellent review on this topic [8].

Carbon nanotubes have attracted a great deal of attention due to their extraordinary electronic, thermal and mechanical properties [18,19] which make them useful materials for applications in electronic devices, catalysis, sensors, field-emission devices and hydrogen-storage media [20,21]. An improvement in conductivity and charge transfer at the electrode interfaces may be expected when carbon nanotubes are used as catalytic support [22] as opposed to a classical support such as carbon black. A significant enhancement in the activity of Pt electrocatalysts toward ORR has been achieved when the nanoparticles are deposited onto single-wall carbon nanotube support [23]. Two main issues are associated with carbon nanotubes: on the one hand, most studies have been conducted with single-wall carbon nanotubes. The price of those is prohibitive for current applications as fuel cell electrocatalyst support; in this sense multi-wall carbon nanotubes

* Corresponding author. Fax: +34 91 585 4760.

E-mail address: srojas@icp.csic.es (S. Rojas).

appear to be a more reasonable (economical) option. On the other hand, due to the lack of surface groups, electrocatalysts synthesized from carbon nanotubes usually have low metal loading, ca. 20 wt% or below [24–27]. Such loading value is rather low for fuel cell applications. Higher metallic loading can be achieved by intermittent microwave irradiation, IMI [28], or surface thiolation [29]; however, both routes involve complicated synthetic approaches. Furthermore, when supported on carbon nanotubes the agglomeration of the metal nanoparticles is also observed [30].

Since CNTs are chemically inert, certain modifications are necessary to incorporate metallic nanoparticles into their structure. Among the plethora of surface functionalization techniques, oxidation is probably the most widely employed. Oxidation of CNTs has been used to remove amorphous carbon for purification [27] and to create functional groups on their surface to favor the anchorage of metallic nanoparticles [31]. The chemical treatment of CNTs is expected to create more sites for metal anchoring, avoiding agglomeration problems while allowing higher metal loading incorporation onto their surface.

In this paper, we report the functionalization of MWCNTs and their application as support for Pt-based electrocatalysts for the oxygen reduction reaction (ORR). The MWCNTs were treated by following two different methodologies and the solids obtained were used as support for anchoring Pt nanosized particles. The Pt nanoparticles supported on the MWCNTs subjected to a severe functionalization treatment are the best cathode material for PEMFC applications, even exceeding the performance of a commercial Pt/C. This fact is related to a higher dispersion of the Pt nanoparticles, which is due to a higher extent of functionalization of the CNTs subjected to the strong oxidation treatment.

2. Experimental procedure

2.1. Functionalization of carbon nanotubes

The functionalization of MWCNTs (CNTs henceforward) has been carried out by means of two different methodologies for studying the influence of the strength of the treatment in the final characteristics of these materials. Both methods involved refluxing the Multi-wall carbon nanotubes (Sunnano®, purity from the provider > 90%, $\varnothing = 10\text{--}30\text{ nm}$) in a mixture of H_2SO_4 (98% Aldrich) and HNO_3 (65% Panreac) for several hours at different temperatures. In the first method, the sulfonitric mixture contained 200 mL of each acid, and the temperature was set at 110°C for 6 h [32]. In the second approach, the sulfonitric mixture was prepared mixing 84 mL of H_2SO_4 and 54 mL of HNO_3 in 280 mL of H_2O , and the temperature was set at 60°C for 2 h [33,34]. After each treatment, ca. 1 L of distilled water was added to the suspension containing each set of nanotubes, being stirred for 12 h. Two sets of nanotubes were obtained by filtration and rinsed with abundant water until the pH of the recovered water was 6. The nanotubes obtained were dried at 100°C for 12 h.

The CNTs obtained with the first methodology were designated as CNT-ST, and those functionalized following the second methodology were designated as CNT-MT in accordance with the severity of the method (ST-severe treatment, MT-mild treatment).

2.2. Synthesis of PtCNT

The preparation of Pt nanoparticles was carried out using polyol technology [27,35]. This method consists in the reduction of metallic precursors in a liquid alcohol medium (ethylene glycol, glycerol, etc.) at moderate temperatures. The alcohol acts as reducing agent and dissolving medium. This method allows for an adequate con-

trol of the size and shape of the nanoparticles through the amount of water added during the synthesis process.

Briefly, an ethylene glycol (EG) solution of the metal precursor (Johnson Matthey H_2PtCl_6) was added dropwise to a suspension of the carbonaceous support (either CNT-ST or CNT-MT) in EG under stirring. Previously, the carbonaceous suspension was stirred and treated in an ultrasonic bath for 30 min. The mixture was stirred for 4 h. Afterwards, a solution of NaOH (2.5 M in EG) was added to adjust the pH to 13. The total amount of water was 5 vol.%. The solution was then refluxed at 140°C for 3 h to ensure the total reduction of the metallic precursors. In this way, Pt nucleation from its salt precursor was accomplished in the presence of the modified support. This process was carried out under flowing N_2 . The solid obtained was thoroughly rinsed with water and dried at 70°C for 8 h; two electrocatalysts, PtCNT-ST and PtCNT-MT, were obtained.

Aliquots of each electrocatalyst were subjected to a temperature-programmed reaction between 25 and 875°C at a rate of 10°min^{-1} under H_2/Ar (10 wt% H_2). Previously, the solid was purged in He at 200°C for 30 min and cooled to 25°C . Four electrocatalysts were obtained and designated PtCNT-ST, PtCNT-MT, PtCNT-ST-875 and PtCNT-MT-875 in accordance with the final reduction temperature and with the carbonaceous support. The commercial 40 wt% Pt/C (Johnson Matthey) was also subjected to thermal treatment at 875°C under the same conditions.

2.3. Physico-chemical characterization

X-ray diffractograms were collected on a Seifert 3000 powder diffractometer, operating with Cu $\text{K}\alpha$ radiation ($\lambda = 0.15418\text{ nm}$) generated at 40 kV and 40 mA. Scans at 0.02°s^{-1} for 2θ values between 10° and 90° were recorded. The display and handling of the diffraction patterns and unit cell refinements (calculated considering all reflections peaks) were carried out using the PowderCell software [36].

X-ray photoelectron spectra (XPS) of the samples were acquired with a VG Escalab 200R spectrometer fitted with an Mg $\text{K}\alpha$ ($h\nu = 1253.6\text{ eV}$) 120 W X-ray source. The energy regions of the photoelectrons of interest were scanned until an acceptable signal-to-noise ratio was achieved. Intensities were estimated by calculating the integral of each peak, determined by subtraction of the Shirley type background and fitting of the experimental curve to a combination of Lorentzian and Gaussian lines of variable proportions. Accurate binding energies ($\pm 0.2\text{ eV}$) were determined by referencing to the C 1s peak at 284.6 eV.

X-ray fluorescence analysis (TXRF) was performed on a Seifert EXTRA-II spectrometer equipped with two X-ray fine focus lines, Mo and W anodes, and a Si(Li) detector with an active area of 80 mm^2 and a resolution of 157 eV at 5.9 keV (Mn $\text{K}\alpha$).

Specimens for transmission electron microscopy (TEM) analysis were prepared by dispersing the powder samples in isobutanol. One drop of the resulting suspension was placed on a perforated carbon film supported by a copper grid. They were studied on a JEM 2100F device equipped with an EDAX detector for X-ray energy dispersive spectroscopy analysis.

Temperature-programmed reduction (TPR) of the catalysts was carried out in a Micromeritics TPD/TPR 2900 unit. Hydrogen consumption was monitored with the aid of a TCD detector and recorded for TPR analysis. These experiments were carried out as described in our previous work [37].

The determination of the nature of the oxygen surface groups in the carbons was accomplished by evolved gas analysis with mass spectrometry (EGA-MS) under Ar. Each sample was heated in an electric furnace at 10°Cmin^{-1} from 30 to 950°C under vacuum ($2.5 \times 10^{-5}\text{ mbar}$). The desorbed products were analyzed by mass spectrometry using a Balzers Prisma TM QMS 200 coupled online to a vacuum system.

Thermogravimetric analysis (TGA) under controlled atmosphere is carried out on a Mettler Toledo TGA/SDTA 851^e, using $200\text{ cm}^3\text{ min}^{-1}$ of N_2 as carrier gas and a rate of $10^\circ\text{C min}^{-1}$.

Textural properties have been evaluated by N_2 adsorption–desorption isotherms of the samples recorded at liquid N_2 temperature with a Micromeritics ASAP 2000 apparatus. Samples were outgassed at 150°C under vacuum for 24 h. Specific areas were calculated by applying the BET method within the complete relative pressure range.

2.4. Electrochemical characterization

The synthesized samples were tested as electrocatalysts for the oxygen reduction reaction. Their performance was compared to that of a commercial 40 wt% Pt/C (Johnson Matthey). Catalytic performance was evaluated by the thin-layer rotating disk electrode (RDE) technique in a conventional three-compartment electrochemical glass cell at 25°C . A glassy carbon rotating disk electrode (0.071 cm^2 , GC-Typ zu628) was used as a substrate for the catalysts. A mercury/mercury sulfate electrode and an Au plate served as the reference and counter electrode, respectively. All potentials are referred to the reversible hydrogen electrode (RHE). A $0.5\text{ M H}_2\text{SO}_4$ (Merck) was used as the electrolyte. All solutions were prepared with Milli-Q water.

The samples under study were deposited onto the working electrode by means of an ink prepared by following a protocol as reported elsewhere [37]. Final Pt loading of each electrode is 9.2, 12.0 and $13.7\text{ }\mu\text{g}$ for PtCNT-ST, PtCNT-MT and Pt/C, respectively. The loadings of PtCNT-ST-875 and PtCNT-MT-875 are 9.2 and $12.0\text{ }\mu\text{g}_{\text{Pt}}$, respectively.

Electrochemical measurements were performed with a potentiostat/galvanostat EG&G 273A controlled by computer. The electrode rotation speed was regulated by a Metrohm 628-10 unit. The rotation rate varied from 500 to 2500 rpm.

Cyclic voltammetry (CV) experiments were conducted to clean and activate the electrode surface. The electrolyte was purged with nitrogen (Air Liquide) for 30 min. The samples were cycled at 100 mVs^{-1} between -0.1 and 1.1 V until reproducible voltammograms were obtained.

Linear sweep voltammetry was used for the study of the oxygen reduction reaction (ORR). The electrolyte was saturated with high purity oxygen (air liquid) for 20 min. The polarization curves were obtained at 2500 rpm between 1.1 and -0.05 V at room temperature.

2.5. Preparation of the membrane electrode assembly (MEA) and performance evaluation in the PEMFC

The catalytic performance of the samples as cathode electrode in a 4 cm^2 single cell was evaluated. The anode catalyst was a commercial 40 wt% Pt/C (Johnson Matthey). The Pt loading in the anode was $0.3\text{ mg cm}^{-2}_{\text{MEA}}$, whereas the Pt loading in the cathode was $0.6\text{ mg cm}^{-2}_{\text{MEA}}$.

A commercial Nafion 113.5 membrane (Dupont) was treated in order to clean and protonate its surface [37,38]. After the treatment, the membrane was dried at room temperature.

A three-layered structure was used to prepare the MEA. Teflon-treated carbon paper (ELAT GDL-LT 1200 W) was used as the backing and gas diffusion layer.

The catalyst layer was sprayed onto the carbon paper by means of an ink. Typically, the ink was formed following the procedure described in our previous works [37,39]. Finally, the MEA was obtained by hot pressing the carbon paper on both sides of the anode–membrane–cathode assembly at 100°C and residual pressing for 3 min [40].

The PEMFC was assembled by mounting the MEA into a 4 cm^2 single cell (Electrochem. Inc.). Each MEA was initially activated at short circuit in H_2/O_2 , keeping the following operation conditions during three cycles of 30 min: H_2 and O_2 : $200\text{ cm}^3\text{ min}^{-1}$ and 3 bar, cell temperature 60°C and no humidity. After the activation process, the performance of the catalysts was tested by feeding hydrogen and oxygen at a flow rate of $200\text{ cm}^3\text{ min}^{-1}$, respectively, a pressure of 3 bar and relative humidity of 60%. Polarization curves were recorded at 80°C by fixing the load current, which was controlled with an electric load system (MITS Pro-FCTS, Arbin Instruments). All single cell tests were conducted three times to ensure the repeatability and reproducibility of the measurements.

3. Results and discussion

3.1. Multi-wall carbon nanotubes

XRD analysis of the carbon nanotubes (either treated or fresh) showed the 002, 100, 004 and 110 diffraction peaks (figure not shown) indicating that the walls of the CNTs are made of graphitic-type stacks. The 002 reflection is more intense for the carbon nanotubes [41–42], than that recorded for Vulcan XC-72R. The intensity of this peak is maintained after the thermal treatment indicating that the order is not affected by this treatment.

It has been reported in the literature that the majority of oxygen-containing groups on carbon supports can be removed from the surface by heating in inert gas between 200 and 1100°C . Semi-quantification of these groups has been accomplished by thermogravimetric analysis. Fig. 1 shows the TGA curves under N_2 atmosphere of the carbon nanotubes. It can be observed that CNT-ST records a larger weight loss than CNT-MT. This feature reflects the presence of a higher amount of functional groups on the surface of the CNT-ST in line with the high strength of the treatment. CNT records the lowest weight of loss in the series followed by CNT-MT. Weight loss in CNT-MT is ca. 4 wt.% reaching a value around 20 wt.% for CNT-ST. This trend reflects that the higher amount of functional groups has been achieved after the severe treatment.

Table 1 shows the value of the BET specific surface area of the different supports. The BET area of CNT-ST is smaller than that of CNT, probably reflecting how the incorporation of functional groups onto its surface blocks the carbon pores. The specific surface area of the CNT-MT is the largest in the series. This fact is related to the mild treatment, which mainly purifies its surface, so the BET area increases due to the lower amount of incorporated functional

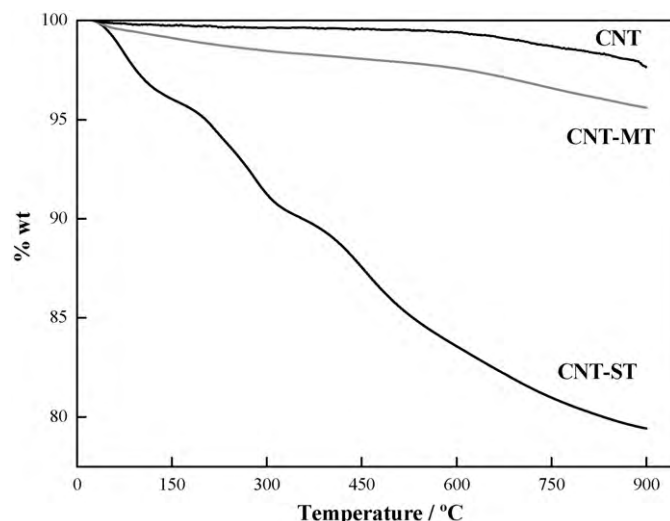


Fig. 1. TGA profiles under N_2 of the carbonaceous supports.

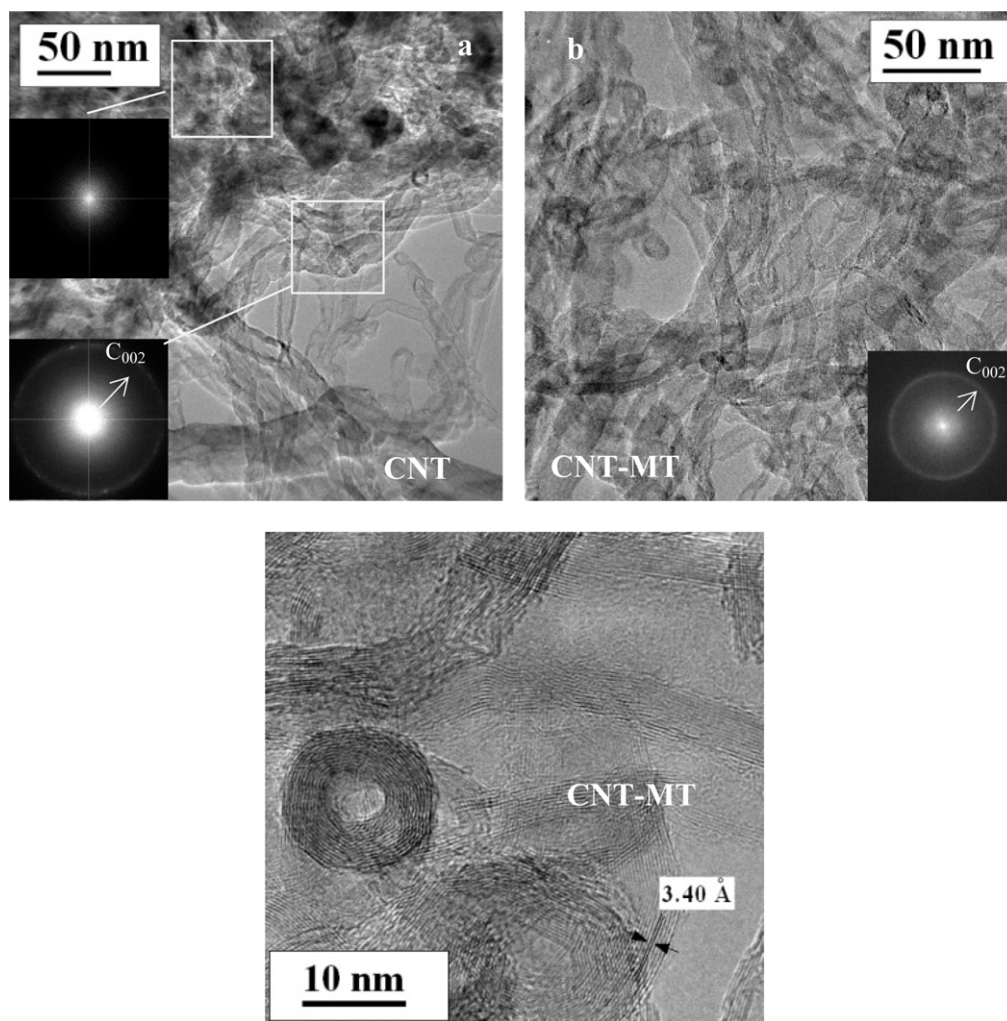


Fig. 2. TEM images of CNT (a) and CNT-MT (b) and HR-TEM image of CNT-MT (c). Amorphous impurities are no longer observed in the latter sample. The insets are the Fast Fourier Transform (FFT) of the TEM images. Impurities are observed in the upper left side of the TEM image of CNT.

groups taken in conjunction with the high elimination of impurities. This observation is in line with the results obtained by Wang and Lu [43], who observed an increase in the BET area in activated carbons treated with HCl, HF and HNO₃ due to the removal of their

Table 1
Characterization data of the CNTs.

Sample	C 1s ^a	O 1s ^a	O/C ^b	BET (m ² g ⁻¹) ^c
CNT	284.3 (45) 285.0 (27) 286.3 (14) 288.0 (4) 290.6 (10)	531.2 (54) 533.4 (46)	0.013	145
CNT-MT	284.3 (45) 285.0 (27) 286.4 (14) 288.0 (3) 290.5 (11)	531.3 (42) 533.1 (58)	0.024	174
CNT-ST	284.2 (41) 285.1 (22) 286.3 (13) 288.1 (9) 290.3 (14)	531.4 (46) 533.3 (54)	0.167	93

^a Binding energies (eV) of core electrons of CNT, CNT-MT and CNT-ST.

^b Atomic ratio determined by XPS.

^c BET specific area.

inorganic constituents. Li et al. [27] also reported a 20% increase in the BET surface area of MWCNT due to the elimination of carbon nanoparticles and carbonaceous impurities after treatment in a sulfonitrilic mixture. The purity of the as-treated MWCNT employed in this paper is 90%. Fig. 2 shows TEM images of CNT and CNT-MT. Amorphous impurities have been removed, or at least are no longer observed, in the latter sample. The insets are the Fast Fourier Transform (FFT) recorded on selected areas of the TEM images in Fig. 2a and b. The bright ring corresponds to the (002) spacings of the graphene sheets of the walls of the carbon nanotubes. Such ring is not observed when the area selected for the FFT analysis is focused on the amorphous impurities, see upper-right corner in Fig. 2a. Fig. 2b depicts an image of the CNT-MT nanotubes recorded at similar magnification than Fig. 2a. The amount of impurities is clearly lower in this sample. The FFT figure also shows the bright ring ascribed to the (002) spacing of the graphene sheets. An HR-TEM image of CNT-MT is shown in Fig. 2c. The multi-wall structure of the material is observed. Concentric graphene sheets showing an interlayer distance of 3.40 Å corresponding to the 002 plane of graphite is shown in the figure. In this figure, CNTs formed by concentric layers of graphene are also observed.

The determination of the nature of the oxygen surface groups was carried out by temperature-programmed evolved gas analysis with mass spectrometry (EGA-MS). Fig. 3 depicts both the CO ($m/z=28$) and CO₂ ($m/z=44$) desorption profiles of the carbon nanotubes. It has been established that the most acidic groups (car-

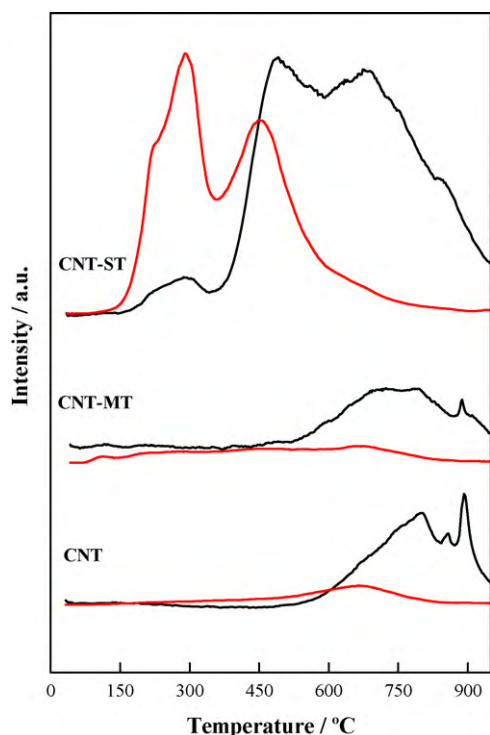


Fig. 3. EGA-MS profiles of fresh CNT, CNT-MT and CNT-ST. The red line corresponds to $m/z = 44$ (CO_2) and the black line corresponds to $m/z = 28$ (CO).

boxylic groups, lactones, anhydrides, etc.) evolved to CO_2 at lower temperatures whereas the least acidic groups (quinones, hydroquinones, ethers, carbonyls, phenols, etc.) evolved to CO at higher temperatures [44,45]. Thus, in the case of CNT-ST, a CO_2 peak results from carboxylic acid at low temperatures (ca. 150–300 °C), and from anhydrides and lactones at higher temperatures (ca. 400–500 °C). A CO peak appears between 400 and 900 °C corresponding to the evolution of phenols, ethers and carbonyl groups. CNT-MT and fresh CNT presented a similar TPD profile. A single broad CO peak indicating the presence of phenols, ether and carbonyl groups is observed. The area of the CO curve in the EGA-MS analysis of the fresh CNT and CNT-MT samples is lower than that of CNT-ST, consistent with a higher amount of functional groups on the latter.

Surface analysis by X-ray photoelectron spectroscopy (XPS) of C 1s, O 1s and S 2p core levels of the nanotubes was carried out. The position and relative abundance of surface species are collected in Table 1. The C 1s spectra were deconvoluted into five components [10]. The peak at ca. 284.6 eV accounts for the presence of graphitic-type carbon (C–C bonds) whereas the peak at ca. 285 eV corresponds to the defects of the carbonaceous sup-

port. Peaks at ca. 286.3 and 288 eV are ascribed to the presence of C–O and C=O species, respectively. The amount of such species is higher in CNT-ST, in line with previous results obtained by EGA-MS and TGA. However, it is difficult to quantify or accurately identify such species. A low intensity broadband around 290.5 eV with $\text{FWHM} \approx 4$ was found in the spectra. Such band is due to a $\pi \rightarrow \pi^*$ transition [46] characteristic of pure graphitic samples and can be taken as an indirect measure of the graphitic character of carbon black [47]. On the other hand, O 1s spectra were deconvoluted into two components. The component located at ca. 531 eV is attributed to C–OH and C=O, whereas the peak at ca. 533 eV is ascribed to COOH [48]. The O/C atomic ratio increases following this trend: $\text{CNT-ST} \gg \text{CNT-MT} > \text{CNT}$.

In line with previous observations, the XPS data confirm that the amount of surface groups on carbon nanotubes increases after chemical treatment and that it can be controlled by the nature of the chemical treatment.

3.2. Electrocatalysts

The activity of the PtCNTs in the ORR has been studied. It is well known that particle size and Pt–Pt interatomic distance play a key role in electrocatalyst performance. In this sense, the studies conclude that higher temperatures increase nanoparticle size, whereas they decrease the Pt–Pt metal distance [49,50]. The importance of thermal treatment in the improvement of electrocatalytic activity in the ORR has been demonstrated [37]. With these considerations in mind, aliquots of the synthesized PtCNTs have been subjected to thermal treatment under H_2/Ar (10 wt% H_2) until a final reduction temperature of 875 °C.

Fig. 4 shows the X-ray diffraction patterns of the electrocatalysts. The presence of Pt fcc could be inferred from strong diffractions at $2\theta = 39.9^\circ$ (1 1 1), 46.3° (2 0 0), 67.7° (2 2 0), 81.3° (3 1 1) and 86.0° (2 2 2). It should be noted that the broad peak centered at ca. $2\theta = 25^\circ$ corresponds to the (0 0 2) diffraction of the carbonaceous support. The diffraction peaks of the electrocatalysts become sharper after thermal treatment (Fig. 4b). This behavior reflects an increase in particle size due to the sinterization of the Pt nanoparticles (Table 2). Admittedly, determining the grain size from the Scherrer equation has the shortcoming of neglecting contributions other than size broadening to the breadth of the reflection. For instance, lattice strain effects, important for nanosized or alloyed particles are neglected [51]. Nevertheless, it is a well-accepted method for the comparison of the crystalline size between similar samples. Furthermore, for the samples studied in this manuscript, the Pt particle size as calculated from the Scherrer equation is in good agreement with the average particle size deduced from TEM analyses (see below).

Remarkably, the increase in Pt size after thermal treatment is higher in PtCNT-MT-875 than in PtCNT-ST-875. This particle size stabilization phenomenon could be explained by

Table 2
Structural parameters of the electrocatalysts.

Sample	Particle size ^a (nm)	Cell parameter (Å)	Pt (%)	Pt/C ^b	Pt ^d /Pt ^c
PtCNT-MT	6.0	3.916 ± 0.002	35 ^d	0.031	63
PtCNT-ST	5.3	3.911 ± 0.004	27 ^d	0.033	61
PtCNT-MT-875	26.5	3.918 ± 0.002	35 ^d	0.015	65
PtCNT-ST-875	19.5	3.918 ± 0.002	27 ^d	0.011	60
Pt/C	3.5	3.908 ± 0.003	42 ^e	0.091	55
Pt/C-875	15.3	3.921 ± 0.002	40 ^e	0.048	57

^a Particle size calculated by Scherrer's equation. The 2 2 0 reflection was selected in order to overcome the contribution of the graphite phase.

^b Atomic ratio determined by XPS.

^c Relative amount (%) of reduced Pt by XPS.

^d Pt content determined by TXRF analysis.

^e The Pt content provided by the supplier (Johnson Matthey) is 40 wt%.

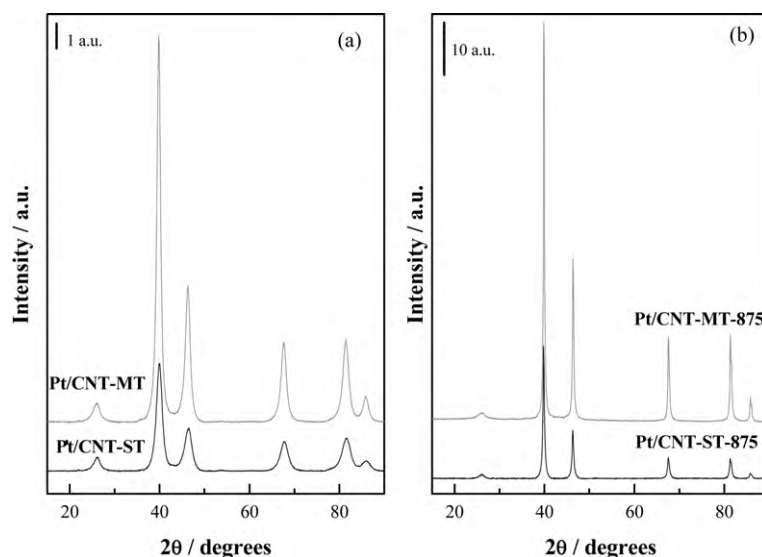


Fig. 4. XRD profiles of (a) fresh electrocatalysts and (b) thermally treated electrocatalysts.

the higher amount of functional groups on the surface of CNT-ST.

Pt dispersion is higher in PtCNT-ST than in PtCNT-MT (see discussion below), so fewer vicinal Pt clusters can interact during thermal treatment to render large aggregates. Furthermore, the strength of the interaction between Pt and CNT is higher when the nanotubes have been subjected to the stronger treatment, which hinders the motion of the Pt centers avoiding their agglomeration [23,49,52]. The lattice parameter of the Pt crystals has been calculated and its value is similar to those obtained for the commercial Pt/C. The samples subjected to thermal treatment present a slightly higher value of the lattice parameter compared to its homologous fresh samples.

Surface analysis by photoelectron spectroscopy of the Pt 4f core level of the electrocatalysts is depicted in Fig. 5. The Pt 4f_{7/2} region contains three peaks whose maxima are centered at 71.4, 72.9 and 75 eV ascribed to Pt⁰, PtO and PtO₂ species [10], respectively. The proportion of each Pt species was practically constant in all samples. Multi-wall carbon nanotubes have been treated to generate surface functional groups since the anchoring of the metallic nanoparticles is favored onto these regions [31]. XPS analyses reveal a similar Pt/C surface ratio on both PtCNT-MT and PtCNT-ST (Table 2). The Pt/C atomic ratio decreases when the electrocatalysts are subjected to thermal treatment, which corresponds to an increase in the particle size, in good agreement with XRD results.

PtCNT-ST and PtCNT-MT record similar nanoparticle size and distribution of metallic species on the nanotube surface. It seems that the only difference may be in the dispersion of the Pt nanoparticles in the carbonaceous support. Transmission electron micrographs of PtCNT-ST and PtCNT-MT are depicted in Fig. 6. The multi-wall structure of the nanotubes can be appreciated in the TEM images, see Fig. 6c. The width of the carbon nanotubes ranges from 5 to 18 nm. Regarding to the distribution and size of the Pt nanoparticles on the nanotube surface, it can be observed how the dispersion of the metallic nanoparticles is higher in PtCNT-ST compared to PtCNT-MT, which presents larger agglomerates of Pt nanoparticles. The mean Pt particle size deduced from TEM analyses varies from 5.2 and 6.5 nm for PtCNT-ST and PtCNT-MT, respectively. This result was obtained after counting 500 particles of different regions of each sample. From these data it is possible to gather information about metal dispersion (D) by applying the

following expression [53]:

$$D = \frac{6M}{\rho \sigma N_A d} \quad (1)$$

Eq. (1) relates metal dispersion to mean particle diameter d (nm). In this equation, M is the platinum atomic weight ($195.08 \text{ g mol}^{-1}$), ρ is Pt density (21.09 g cm^{-3}), σ is the surface covered by one exposed platinum atom ($0.089 \text{ nm}^2/\text{at}$) [54] and N_A is the Avogadro constant ($6.022 \times 10^{23} \text{ at/mol}$). The value of the dispersion calculated in this way varies from 0.20 to 0.16 for PtCNT-ST and PtCNT-MT, respectively.

At first, one might think that the better nanoparticle dispersion obtained in PtCNT-ST could be related to its lower amount of Pt compared to PtCNT-MT (27 wt% Pt vs. 35 wt% Pt, listed in Table 1). In principle, the ability of carbon supports to facilitate high dispersion of metal particles could be ascribed to the presence of acidic oxygen-containing groups at the edges of graphene networks [55,56]. Suh et al. reported that carboxylic groups on the carbon surface avoid the migration of metal nanoparticles, favoring the increase in metal dispersion due to an increase in the number of sites for the formation of nuclei [57]. They found that more acidic groups have a major influence on metal dispersion by providing nucleating sites and enhancing the hydrophilicity of the carbon surface. Prado-Burguete et al. observed that an increase in the metal–carbon interaction could hinder the sintering of the metal particles [52]. They proposed that a decrease in carbon hydrophobicity could enhance the diffusion of the metal precursors toward the internal porosity of the carbons during the synthetic procedure in polar solutions, therefore giving a better dispersion. This decrease in carbon hydrophobicity is caused mainly by the carboxylic groups. On the other hand, they proposed that the more effective sites for the anchorage of Pt nanoparticles are the less acidic groups due to their high stability, although according to a commonly accepted mechanism [55], the low acidity of both functional groups would not avoid the sintering of metal particles. Once accepted that oxygen-containing groups behave as anchors for Pt particles, increasing their dispersion, it is easy to explain the higher dispersion of PtCNT-ST compared to PtCNT-MT. The amount of functional groups (carboxylic, phenols, etc) is far superior in PtCNT-ST compared to PtCNT-MT.

On the other hand, the same synthetic procedure has been followed to prepare the PtCNTs catalysts considered in this paper. The

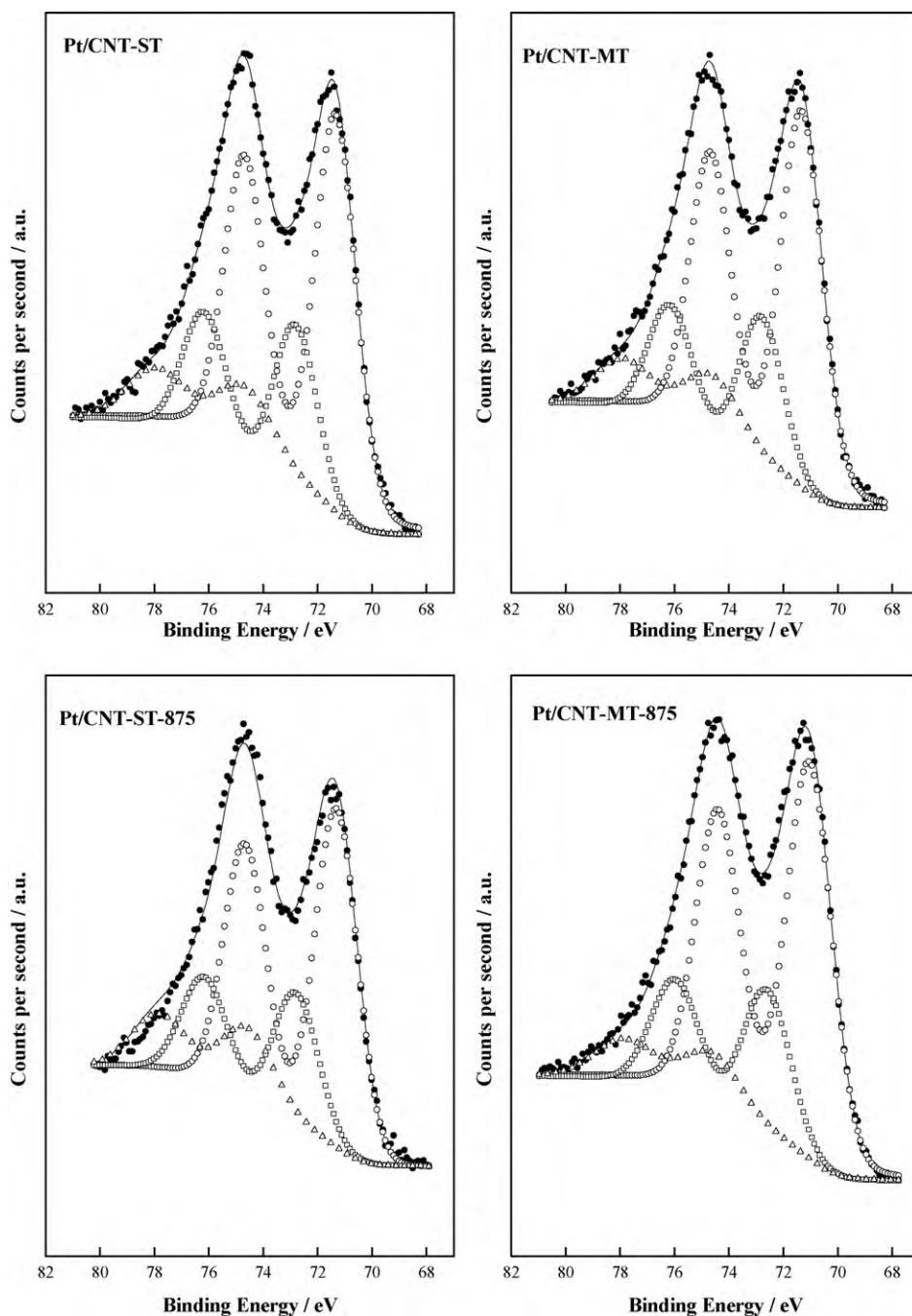


Fig. 5. XPS Pt 4f core level spectra of the electrocatalysts. Pt⁰ (○), Pt^{II} (□) and Pt^{IV} (△).

total amount of Pt varied from 27 wt% to 35 wt% for PtCNT-ST and PtCNT-MT, respectively. Some authors suggested that the adsorption of the metal ions decreased when oxidized or graphitized carbons are used, suggesting that the surface oxygen-containing groups and the basal planes of carbon crystallites play a minor role in this process [58,59]. On the other hand, the adsorbed ionic metal species tends to form complexes with oxygen-free sites on the carbon surface [59]. It is well established that the unsaturated C–C bonds (called C_{π} sites) determine the formation of Pt–C [60]. There are three types of C_{π} sites: sites of weak, strong and irreversible adsorption. The concentration of these sites decreases upon destruction of the surface $>C=C<$ groups by means of oxidation, especially the sites of strong and irreversible adsorption. In most cases, the sites of strong adsorption dominate the syn-

thesis of carbon supported samples. The functionalization degree of CNT-ST is far superior to that of CNT-MT. Therefore, in line with previous discussion the lower Pt loading of PtCNT-ST could be explained by the lesser amount of strong adsorption sites on CNT-ST. The XPS analysis revealed that the amount of $>C=C<$ (BE of ca. 290.3 eV) species represents 11% and 4% with regard to the total amount of carbon species for PtCNT-MT and PtCNT-ST, respectively.

Both $>C=C<$ and oxygen-containing sites on the carbon surface are responsible for Pt–C interaction. Although the interaction of Pt on the C_{π} sites is favored, its strength is higher on the oxygen-containing sites. In this sense, PCNT-ST has a higher amount of functional groups on its surface as compared to PtCNT-MT, so Pt–C interaction will be stronger, avoiding the sinterization of the

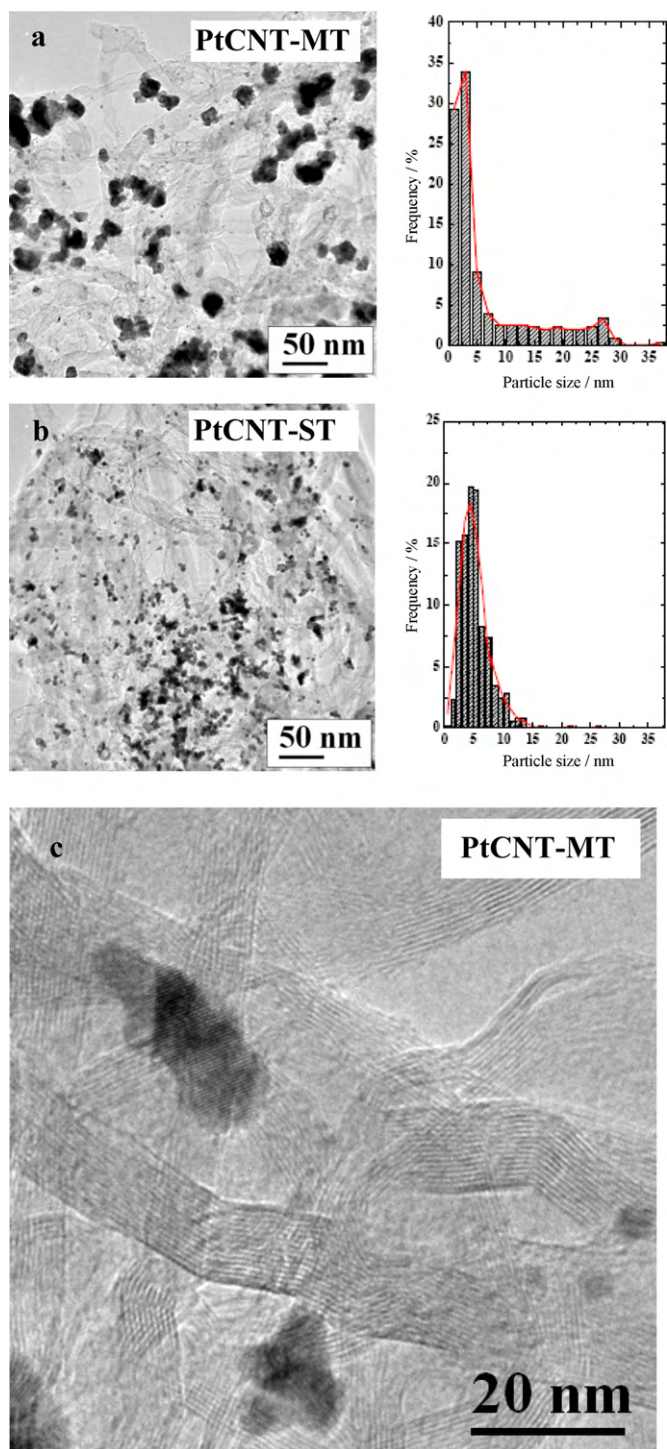


Fig. 6. TEM micrographs showing particle size distribution histograms of PtCNT-ST and PtCNT-MT. HR-TEM image of PtCNT-MT (c) shows the multi-wall structure of the nanotubes.

nanoparticles and increasing their dispersion. On the other hand, the amount of $>C=C<$ species is lower in PtCNT-ST, so Pt loading in the catalyst will be lower as compared to PtCNT-MT.

Although not described, the as received CNTs were also used as support for Pt incorporation by following the same protocol as that used for the chemically treated nanotubes. The amount of Pt incorporated on this sample, as deduced from ICP analysis, was 22 wt%. This value is below the 40 wt% aimed in this study, but in line with previous reports dealing with non-functionalized CNTs

[24–27]. As a consequence, no further studies were conducted on this sample.

The behavior of the electrocatalysts in the ORR and their performance in a single cell was investigated. Fig. 7a depicts the cyclic voltammograms for the fresh electrocatalysts. Features of the hydrogen adsorption–desorption region between 0 and 0.40 V, followed by the “double layer” potential region, can be observed. OH adsorption and oxide formation take place at potential >0.70 V in PtCNT-ST, whereas in PtCNT-MT they start at potentials >0.73 V. A negative current peak corresponding to oxide reduction is centered at potentials of 0.81 and 0.84 V for the PtCNT-ST and PtCNT-MT, respectively. This shift of ca. 30 mV can be ascribed to the oxophilicity of the samples [61]. PtCNT-MT is less oxophilic than PtCNT-ST, so the formation of OH species that block the O_2 adsorption sites is hindered in the former. The voltammograms of PtCNT-ST depict another small oxide formation peak at ca. 0.6 V, which could be ascribed to the oxidation of the surface oxides of the support [12].

Fig. 7b depicts the j - E data obtained from linear sweep voltammetry (LSV) experiments recorded at 2500 rpm and 1 mV s^{-1} in O_2 saturated 0.5 M H_2SO_4 solutions on the different electrocatalysts. The onset for the ORR is shifted towards more positive potentials in the samples subjected to thermal treatment (listed in Table 3). However, the performance of PtCNT-ST throughout the polarization range is the best of the series for the ORR, displaying lower overpotentials in the kinetic and mixed controlled regions.

The distinct ability of the electrocatalysts to reduce O_2 could be related to such features as sample oxophilicity, preferential orientation of the crystals or particle size. On the one hand, the cyclic voltammograms of the samples depicted in Fig. 7a reveal the presence of adsorption states associated to $\{110\}$ and $\{100\}$ facets at ca. 0.08 and 0.22 V, respectively. It has been reported that the $\{100\}$ crystal face of Pt nanoparticles is the most active one for the oxygen reduction reaction [12,62]. The peak associated to the $\{100\}$ facet is similar in both PtCNT-ST and PtCNT-MT, hence the superior performance of the former in the ORR cannot be attributed to the preferential orientation of Pt particles on that sample. On the other hand, it is well known that the ORR is favored on highly dispersed Pt particles with an average particle size of between 3.5 and 5.5 nm [12,63]. Furthermore, the higher dispersion and particle size of PtCNT-ST, 5.2 nm as measured by TEM, make it a more suitable electrocatalyst for the ORR than PtCNT-MT.

The number of electrons involved in the ORR has been calculated using the Koutecky–Levich analysis of the LSV data recorded at different rotation rates (500–2500 rpm) for PtCNT-MT and PtCNT-ST. The total current i during the oxygen reduction reaction can be expressed as:

$$\frac{1}{i} = \frac{1}{i_k} + \frac{1}{i_d} \quad (2)$$

where i_d is the diffusion limited current and i_k is the kinetic current. For the RDE studies, the diffusion current is a function of rotation speed, and it should obey the Levich equation:

$$i_d = 0.62nFAC_0D_0^{2/3}\nu^{-1/6}\omega^{1/2} = B\omega^{1/2} \quad (3)$$

The number of electrons transferred for each O_2 molecule has been estimated by assuming $C_{O_2} = 1.1 \times 10^{-3} \text{ M}$, $D_{O_2} = 1.9 \times 10^{-5} \text{ cm}^2 \text{ s}^{-1}$ and $\nu = 1.009 \times 10^{-2} \text{ cm}^2 \text{ s}^{-1}$ [64], and knowing the geometric electrode surface, rotation speed and Faraday constant.

Both PtCNT-ST and PtCNT-MT go through a mixed mechanism, $n=3.3$ (Eqs. (4) and (5)).



The values of the Tafel slopes at low and high overpotential are 0.060 and 0.114 V/dec for PtCNT-MT, and 0.055 and 0.115 V/dec for

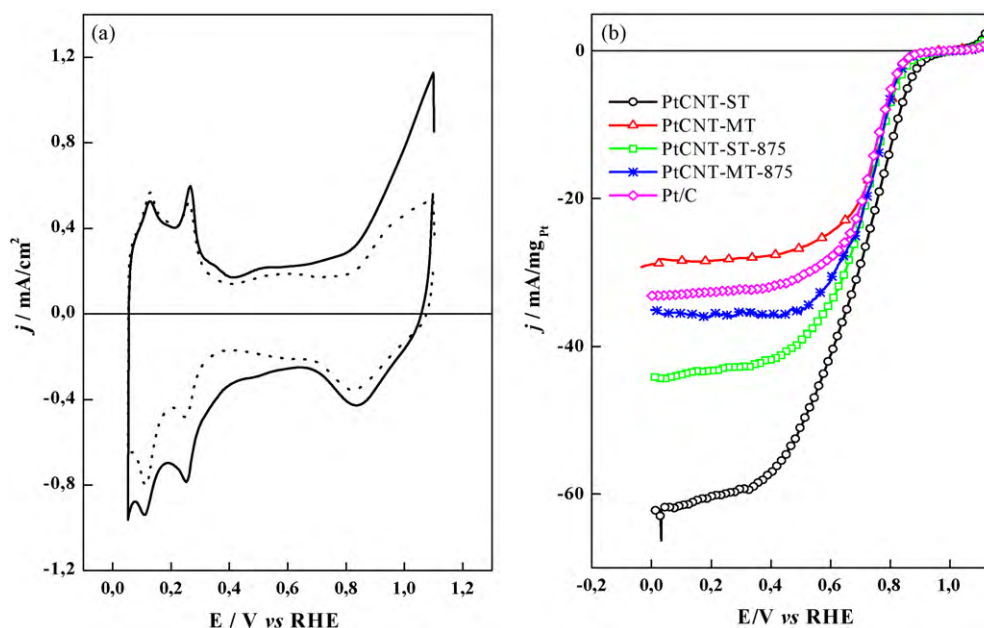


Fig. 7. (a) Cyclic voltammograms for Pt/CNT-ST (dotted line) and Pt/CNT-MT (straight line). Curves were recorded at 10 mV s^{-1} sweep rate in N_2 saturated $0.5 \text{ M H}_2\text{SO}_4$ at room temperature; (b) linear sweep voltammetry (LSV) recorded at 1 mV s^{-1} , in O_2 saturated $0.5 \text{ M H}_2\text{SO}_4$ at 2500 rpm for Pt/CNT-ST (black circles), Pt/CNT-MT (red triangles), Pt/CNT-ST-875 (green squares), Pt/CNT-MT-875 (blue asterisks) and Pt/C (pink diamond). (For interpretation of the references to color in this figure legend, the reader is referred to the web version of the article.)

Pt/CNT-ST, respectively. These values are in accordance with results reported for the ORR on Pt-Vulcan, where Tafel slopes of ca. 2.3 RT/F and $2 \times 2.3 \text{ RT/F}$ were obtained at low and high overpotentials, respectively [65]. However, in the case of the electrocatalysts subjected to thermal treatment, the Tafel slopes decrease, especially at high overpotential (see Table 3). It is well known that Temkin conditions are upheld only in a narrow range of the electrode potential. According to the increase in the reaction rate, the coverage by reaction intermediates decreases, and Langmuir conditions prevail [66]. The change of slope from low to high overpotential reflects the change in the extent of adsorption of reaction intermediates. Consequently, a significant change is brought about in the parameters for the ORR.

A drawback to the electrochemical testing of electrocatalysts is that the conclusions drawn from them do not always correspond to the performance of the samples in real fuel cell conditions. Therefore, the performance of the electrocatalysts in a single fuel cell has been evaluated. The results are shown in Fig. 8, revealing that Pt/CNT-ST is a better cathode material than Pt/CNT-MT and the commercial sample used as reference. Throughout the polarization range, Pt/CNT-ST records the higher current density. The maximum power density recorded for Pt/CNT-ST is 490 mW cm^{-2} , as compared to 450 and 310 mW cm^{-2} recorded for Pt/C and Pt/CNT-MT respectively. This result is in good agreement with the electrochemical experiments for the performance of the different catalysts for the ORR reported in Fig. 7. It is however difficult to compare the performance of the catalysts reported in this manuscript with

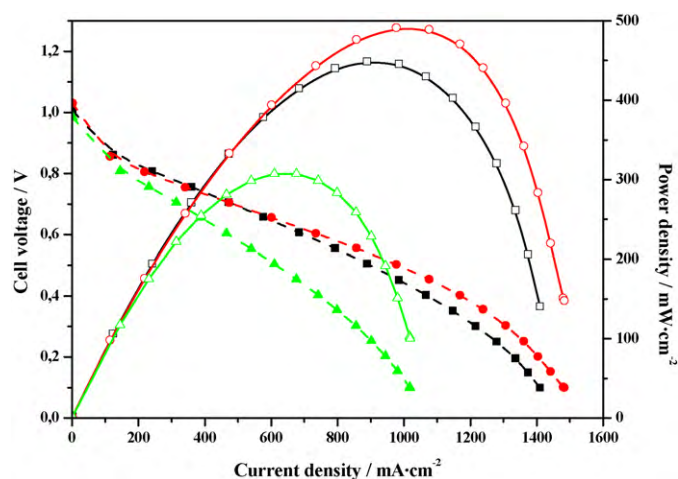


Fig. 8. Polarization (filled symbols) and power density curves (open symbols) of Pt/C (black squares), Pt/CNT-ST (red circles) and Pt/CNT-MT (green triangle) as cathode in H_2/O_2 at 80°C . The anode catalyst was a commercial Pt/C sample (Johnson Matthey). Pt loading was 0.3 and $0.6 \text{ mg cm}^{-2} \text{ MEA}$ for anode and cathode, respectively. (For interpretation of the references to color in this figure legend, the reader is referred to the web version of the article.)

Table 3
Kinetic values in the ORR of the samples.

Sample	E_{ORR} (mV) ^a	j at $E = 0.7 \text{ V}^b$ (mA/mg _{Pt})	j at $E = 0.8 \text{ V}^b$ (mA/mg _{Pt})	Tafel slope (V/dec) ^c LO/HO
Pt/CNT-MT	947	19.8	7.1	0.060/0.114
Pt/CNT-ST	1002	28.8	13.1	0.055/0.155
Pt/CNT-MT-875	1007	22.8	6.2	0.052/0.090
Pt/CNT-ST-875	1011	23.0	10.1	0.052/0.101

^a Onset of the ORR.

^b Current densities measured at 2500 rpm and 1 mV s^{-1} in the ORR.

^c LO: low overpotential and HO: high overpotential.

others previously reported due to the scatter experimental conditions reported by other groups. For instance Rajalakshmi et al. [31] report a voltage of 676 mV at 500 mA cm⁻². At the same current density PtCNT-ST records a voltage of 695 mV. A voltage of 470 mV at 300 mA cm⁻² is reported in Ref. [24] for the performance of Pt supported on functionalized multi-walled carbon nanotubes using Nafion 113.5. Under the same conditions, PtCNT-ST records a voltage of 770 mV.

Taking all the experimental results obtained into account, PtCNT-ST is the best cathode material in the series for PEMFC applications, even outperforming commercial Pt/C. The particle size of PtCNT-ST derived from TEM analysis is 5.2 nm (see above), pretty similar to that of the commercial catalyst. Its superior performance can reflect better particle dispersion or to a positive effect of the support since due to its higher hydrophilicity it can facilitate water management and the access of the humidified reactants to the active sites.

4. Conclusions

Multi-walled carbon nanotubes have been functionalized by oxidation in acid medium and used as support for the incorporation of Pt nanoparticles. The functionalization degree of the nanotubes can be controlled by modifying the treatment protocol. When subjected to severe functionalization treatment, lesser sites for Pt adsorption are available. However, the strength of those sites is higher than that of those remaining in the nanotubes subjected to mild treatment. This feature justifies the lower amount of Pt deposited on CNT-ST but their higher dispersion and lower mobility, impeding their agglomeration when subjected to thermal treatment in hydrogen. PtCNT-ST results in the best electrocatalyst for the oxygen reduction reaction as deduced from the electrochemical studies. Furthermore, single cell experiments reveal that the performance of PtCNT-ST is also superior to that of PtCNT-MT and Pt/C commercial catalysts as the cathode electrode in a proton-exchange membrane fuel cell.

Acknowledgements

The Comisión Interministerial de Ciencia y Tecnología (CICYT) project reference CTQ-2007-66547/BQU is acknowledged for financial support. M. Montiel thanks the CAR for a grant. S. Rojas acknowledges the CSIC Project 200780I017.

References

- [1] H.A. Gasteiger, S.S. Kocha, B. Sompalli, F.T. Wagner, *Appl. Catal. B: Environ.* 56 (2005) 9–35.
- [2] B. Moreno, E. Chinarro, J.L.G. Fierro, J.R. Jurado, *J. Power Sources* 169 (2007) 98–102.
- [3] W.J. Lee, M. Alhosan, S.L. Yohe, N.L. Macy, W.H. Smyrl, *J. Electrochem. Soc.* 155 (2008) B915–920.
- [4] S.H. Kang, T.-Y. Jeon, H.-S. Kim, Y.-E. Sung, W.H. Smyrl, *J. Electrochem. Soc.* 155 (2008) B1058–1065.
- [5] J.L. Gómez de la Fuente, M.V. Martínez-Huerta, S. Rojas, P. Terreros, J.L.G. Fierro, M.A. Peña, *Catal. Today* 116 (2006) 422–432.
- [6] M.V. Martínez-Huerta, S. Rojas, J.L. Gómez de la Fuente, P. Terreros, M.A. Peña, J.L.G. Fierro, *Appl. Catal. B: Environ.* 69 (2006) 75–84.
- [7] J.L. Gómez de la Fuente, M.V. Martínez-Huerta, S. Rojas, P. Hernández-Fernández, P. Terreros, J.L.G. Fierro, M.A. Peña, *Appl. Catal. B: Environ.* 88 (2009) 505–514.
- [8] E. Antolini, *Appl. Catal. B: Environ.* 88 (2009) 1–24.
- [9] T.S. Ahmadi, Z.L. Wang, T.C. Green, A. Henglein, M.A. El-Sayed, *Science* 272 (1996) 1924–1926.
- [10] J.L. Gómez de la Fuente, S. Rojas, M.V. Martínez-Huerta, P. Terreros, M.A. Peña, J.L.G. Fierro, *Carbon* 44 (2006) 1919–1929.
- [11] N.M. Markovic, P.N. Ross Jr., *Surf. Sci. Rep.* 45 (2002) 117–129.
- [12] M. Peuckert, T. Yoneda, R.A. Dalla Betta, M. Boudart, *J. Electrochem. Soc.* 133 (1986) 944–947.
- [13] G.Q. Sun, J.T. Wang, R.F. Savinell, *J. Appl. Electrochem.* 28 (1998) 1087–1093.
- [14] S. Baranton, C. Coutanceau, C. Roux, F. Hahn, J.-M. Léger, *J. Electroanal. Chem.* 577 (2005) 223–234.
- [15] R. Bashyam, P. Zelenay, *Nature* 443 (2006) 63–66.
- [16] S. Von Kraemer, K. Winkander, G. Lindbergh, A. Ulundblad, A.E.C. Palmqvist, *J. Power Sources* 180 (2008) 185–190.
- [17] J. Marie, R. Chenitz, M. Chatenet, S. Berthon-Fabry, N. Cornet, P. Achard, *J. Power Sources* 190 (2009) 423–434.
- [18] R.A.H. Niessen, J. de Jonge, P.H.L. Notten, *J. Electrochem. Soc.* 153 (2006) A1484–1491.
- [19] M.S. Dresselhaus, G. Dresselhaus, P. Avouris, *Carbon Nanotubes: Synthesis, Structure, Properties and Applications*, Springer-Verlag, New York, 2001.
- [20] J.M. Planeix, N. Coustel, B. Coq, V. Brotons, P.S. Kumbhar, R. Dutartre, P. Geneste, P. Bernier, P.M. Ajayan, *J. Am. Chem. Soc.* 116 (1994) 7935–7936.
- [21] P.M. Ajayan, S. Iijima, *Nature* 361 (1993) 333–334.
- [22] G. Girishkumar, M. Rettker, R. Underhile, D. Binz, K. Vinodgopal, P. McGinn, P. Kamat, *Langmuir* 21 (2005) 8487–8494.
- [23] A. Kongkanand, S. Kuwabata, G. Girishkumar, P. Kamat, *Langmuir* 22 (2006) 2392–2396.
- [24] M.M. Shaijumon, S. Ramaprabhu, N. Rajalakshmi, *Appl. Phys. Lett.* 88 (2006) 31051–31053.
- [25] J. Prabhuram, T.S. Zhao, Z.K. Tang, R. Chen, Z.X. Liang, *J. Phys. Chem. B* 110 (2006) 5245–5252.
- [26] A.L. Ocampo, M. Miranda-Hernández, J. Morgabo, J.A. Montoya, P.J. Sebastian, *J. Power Sources* 160 (2006) 915–924.
- [27] W. Li, C. Liang, W. Zhou, J. Qiu, Z. Zhou, G. Sun, Q. Xin, *J. Phys. Chem. B* 107 (2003) 6292–6299.
- [28] Z.Q. Tian, S.P. Jiang, Y.M. Liang, P.K. Shen, *J. Phys. Chem. B* 110 (2006) 5343–5350.
- [29] Y.-T. Kim, T. Mitani, *J. Catal.* 238 (2006) 394–401.
- [30] Z. Liu, X. Lin, J.Y. Lee, W. Zhang, M. Han, M.L. Gan, *Langmuir* 18 (2002) 4054–4060.
- [31] N. Rajalakshmi, H. Ryu, M.M. Shaijumon, S. Ramaprabhu, *J. Power Sources* 140 (2005) 250–257.
- [32] Y. Lin, X. Cui, X. Ye, *Electrochem. Commun.* 7 (2005) 267–274.
- [33] Y. Xing, *J. Phys. Chem. B* 108 (2004) 19255–19259.
- [34] Y. Xing, L. Li, C.C. Chusuei, R.V. Hull, *Langmuir* 21 (2005) 4185–4190.
- [35] D. Larcher, R. Patrice, *J. Solid State Chem.* 154 (2000) 405–411.
- [36] W. Kraus, G. Nolze, *J. Appl. Crystallogr.* 29 (1996) 301–303.
- [37] P. Hernández-Fernández, S. Rojas, P. Ocón, J.L. Gómez de la Fuente, P. Terreros, M.A. Peña, J.L.G. Fierro, *Appl. Catal. B: Environ.* 77 (2007) 19–28.
- [38] K. Makino, K. Furukawa, K. Okajima, M. Sudoh, *Electrochim. Acta* 51 (2005) 961–965.
- [39] P. Hernández-Fernández, S. Rojas, P. Ocón, A. de Frutos, J.M. Figueroa, P. Terreros, M.A. Peña, J.L.G. Fierro, *J. Power Sources* 177 (2008) 9–16.
- [40] Z. Qi, A. Kaufman, *J. Power Sources* 113 (2003) 37–43.
- [41] J.H. Zhou, Z.J. Sui, P. Li, D. Chen, Y.C. Dai, W.K. Yuan, *Carbon* 44 (2006) 3255–3262.
- [42] J.-P. Tessonnier, D. Rosenthal, T.W. Hansen, C. Hess, M.E. Schuster, R. Blume, F. Girgsdies, N. Pfänder, O. Timpe, D.S. Su, R. Schlögl, *Carbon* 47 (2009) 1779–1798.
- [43] S. Wang, G.Q. Lu, *Carbon* 36 (1998) 283–292.
- [44] G.S. Szymanski, Z. Karpinski, S. Biniak, A. Swiatkowski, *Carbon* 40 (2002) 2627–2639.
- [45] J.L. Gómez de la Fuente, M.V. Martínez-Huerta, S. Rojas, P. Terreros, J.L.G. Fierro, M.A. Peña, *Carbon* 43 (2005) 3002–3005.
- [46] H. Estrade-Szwarczkopf, *Carbon* 42 (2004) 1713–1721.
- [47] D. Pantea, H. Darmstadt, S. Kaliaguine, C. Roy, *Appl. Surf. Sci.* 217 (2003) 181–193.
- [48] D.Q. Yang, J.F. Rochette, E. Sacher, *J. Phys. Chem. B* 109 (2005) 7788–7794.
- [49] E. Antolini, *Mat. Chem. Phys.* 78 (2003) 563–573.
- [50] M. Min, J. Cho, K. Cho, H. Kim, *Electrochim. Acta* 45 (2000) 4211–4217.
- [51] J. Weismüller, in: A.S. Edelstein, R.C. Cammarata (Eds.), *Nanomaterials: Synthesis, Properties and Applications*, Institute of physics publishing Bristol and Philadelphia, 2002, pp. 230–249.
- [52] C. Prado-Burguete, A. Linares-Solano, F. Rodríguez-Reinoso, C. Salinas-Martínez de Lecea, *J. Catal.* 115 (1989) 98–106.
- [53] C. Force, A. Ruiz Paniego, J.M. Guil, J.M. Gatica, C. López-Cartes, S. Bernal, J. Sanz, *Langmuir* 17 (2001) 2720–2726.
- [54] P. Panagiotopoulou, D.I. Kondarides, *J. Catal.* 225 (2004) 327–336.
- [55] W.M.H. Sachtler, A.Y. Stakheev, *Catal. Today* 12 (1992) 283–295.
- [56] S.V. Gurevich, P.A. Simonov, A.S. Lisitsyn, V.A. Likhonobov, E.M. Moroz, A.L. Chuvilin, V.N. Kolomiichuk, *React. Kinet. Catal. Lett.* 41 (1990) 211–216.
- [57] D.J. Suh, T.J. Park, S.K. Ihm, *Carbon* 31 (1993) 427–435.
- [58] G.C. Torres, E.L. Jablonski, G.T. Baronetti, A.A. Castro, S.R. de Miguel, O.A. Scelza, *Appl. Catal. A* 161 (1997) 213–226.
- [59] P.A. Simonov, A.V. Romanenko, I.P. Prosvirin, G.N. Kryukova, A.L. Chuvilin, S.V. Bogdanov, E.M. Moroz, V.A. Likhonobov, in: G. Poncelet (Ed.), *Preparation of Catalysts VII*, Stud. Surf. Sci. Catal., vol. 118, Elsevier, Amsterdam, 1998, p. 15.
- [60] A. Wieckowski, E.R. Savinova, C.G. Vayenas, *Catalysis and Electrocatalysis at Nanoparticle Surfaces*, Marcel Dekker Inc., New York, 2003, chapter 12, pp. 428.
- [61] K.J.J. Mayrhofer, B.B. Blizanac, M. Arenz, V.R. Stamenkovic, P.N. Ross, N.M. Markovic, *J. Phys. Chem. B* 109 (2005) 14433–14440.
- [62] K. Kinoshita, *J. Electrochem. Soc.* 137 (1990) 845–848.
- [63] M.L. Sattler, P.N. Ross, *Ultramicroscopy* 20 (1986) 21–28.
- [64] T.J. Schmidt, H.A. Gasteiger, G. Stäb, P. Urban, D.M. Kolb, R.J. Behm, *J. Electrochem. Soc.* 145 (1998) 2354–2358.
- [65] U.A. Paulus, T.J. Schmidt, H.A. Gasteiger, R.J. Behm, *J. Electroanal. Chem.* 495 (2001) 134–145.
- [66] A. Damjanovic, M.A. Genshaw, *Electrochim. Acta* 15 (1970) 1281–1283.